scientific reports



OPEN

Machine learning analysis of a Fano resonance based plasmonic refractive index sensor using U shaped resonators

Shiva Khani[™], Pejman Rezaei & Mohammad Rahmanimanesh

Plasmonic sensors have received special consideration for refractive index (RI) measurement due to the benefits of compact footprints and high sensitivities. To fulfill such conditions, a Fano resonance (FR)-based RI sensor using plasmonic nano-structures is designed and analyzed here. The presented topology comprises a metal–insulator–metal waveguide, a U-shaped, and an inverted U-shaped resonator. The transmission spectrum is obtained utilizing the finite-difference time-domain method. Two FRs appear in the transmission spectrum that are suitable options for sensing performance. The best values of two important factors are a sensitivity of 571.4 nm/RIU and a figure of merit of 14,987 RIU⁻¹ for the first FR (598 nm). Furthermore, the transmittance values at intermediate wavelengths with four geometrical parameters and the RI of the analyte are predicted utilizing the Extreme Randomized Tree regression model. This model is evaluated utilizing an adjusted R square score (Adj-R²S) as an assessment parameter using the value of n_{min} = 3 and a test case of 10%. The Adj-R²S closes 1, showing that transmittance values can be forecasted with high precision. Applying this method decreases the simulation time and resources by 90%. The presented sensor with machine learning behavior prediction ability can be utilized for RI sensing performance.

In recent years, due to the fast progress of novel information technology, the requirement for increased integration density in photonic instruments has increased quickly¹. Transverse electromagnetic (EM) waves spreading along the metal–insulator junction with declining amplitude are called surface plasmon polaritons (SPPs)²-⁴. Since surface plasmon-based structures have unbelievable features, such as manipulating light at a sub-wavelength scale and overcoming the diffraction limit, they have been widely utilized in different applications⁵-7. In the past few years, researchers have proposed numerous optical devices using SPP structures such as plasmonic filters^{8,9}, demultiplexers¹0-12, splitters¹3,1⁴, sensors¹5-17, couplers¹8, absorbers¹9,20, modulators²1,22, logic gates²3,2⁴, switches²5,26, and so on.

Plasmonic refractive index (RI) sensors have attracted exceptional consideration for detecting RI changes in materials^{27,28}. This is because of their high sensitivity to their surrounding medium and local field increment²⁹. Till now, researchers have designed and investigated numerous surface plasmon-based sensors using various structures and resonator shapes. In³⁰, a plasmonic RI sensor (RIS) using a rectangular resonator incorporating metal nanorods with two baffles and a metal–insulator–metal (MIM) plasmonic waveguide (WG) for biological applications is proposed. In this structure, the sensitivity is 2963.73 nm/RIU, and the figure of merit (FoM) equals 5.1 RIU⁻¹. In another approach³¹, a nano-plasmonic structure for RI and temperature sensing is designed. The suggested structure comprises a stub cavity, a ring-shaped cavity with a stub, and an MIM plasmonic WG. Its transmission curve has a Fano resonance (FR) mode produced by the interaction between the transmission spectra of the ring-shaped cavity and the stub cavity. The sensitivity and FoM are 1420 nm/RIU, and 76.76 RIU⁻¹, respectively. Also, its temperature sensitivity is 0.8 nm/°C.

Other resonator shapes that have been used to design sensor structures are circular resonators. A plasmonic sensor utilizing two circular resonators and an MIM WG is designed in³². The sensor structure proposed is used for temperature and RI sensing with the temperature and RI sensitivity values of 0.336 nm/°C and 737.71 nm/ RIU, respectively. In³³, a surface plasmon-based sensor is presented by coupling an MIM plasmonic WG to a U-shaped ring resonator with three stub resonators. This topology generates a band stop spectrum for sensing applications with a sensitivity of 2900 nm/RIU and a FoM of 55.76 RIU⁻¹. It is worth mentioning that there are

Faculty of Electrical and Computer Engineering, Semnan University, Semnan, Iran. [™]email: shiva.khani@semnan.ac.ir

other various structures for designing plasmonic sensors such as elliptical resonators³⁴, split ring resonators³⁵, triangular resonators³⁶, and so on.

It is worth noting that various structures proposed for optical sensors can generate different transmission spectrum shapes. For example, by coupling two plasmonic WG to a resonator from both sides, a bandpass spectrum is formed³⁷, and a bandstop spectrum is formed by coupling one plasmonic WG to a resonator from one side³⁸. Furthermore, stub-coupled MIM WG systems can produce a Plasmon-induced transparency (PIT) spectrum³⁹. Another transmission spectrum type is the FR spectrum caused by interference between two scattering amplitudes⁴⁰. The first is because of scattering within a continuum of states (the background process), and the other is caused by an excitation of a discrete state (the resonant process).

To increase the sensitivity of plasmonic sensors with bandpass, bandstop, and PIT resonance modes, the quality factor (Q-factor) of such modes must be increased. To achieve a high Q-factor value, the resonance mode bandwidth should be as narrow as possible³⁴ which has some challenges. The first is that reducing bandwidth is possible to some extent, as it has effects such as increasing losses and reducing resonance transmittance. Also, this issue needs high fabrication accuracy which complicates the fabrication process. Since the transmission spectrum of an FR mode is an asymmetric line and usually has one transient edge, achieving a high-sensitivity sensor with an FR spectrum is easier than sensors with other types of spectra. Therefore, this paper uses a plasmonic structure that can produce an FR spectrum.

Most referenced optical plasmonic sensors have been analyzed using EM simulation software, which is based on time-consuming and repetitive techniques including finite element method (FEM) and finite-difference time-domain (FDTD) method. Using such numerical methods involves extensive trial-and-error searches over structural dimensions. Accordingly, each parameter must be validated and optimized. For this purpose, utilizing machine learning (ML) methods such as regression analysis and neural networks is important ^{41–43}. ML methods can show the behavior of optical sensors by predicting their transmittance. The relationship between the independent and dependent parameters (wavelength and transmittance) can be observed by regression analysis. Furthermore, to specify patterns over time under various situations, transmittance values or frequency responses, which are data variables, are analyzed with time series analysis. As a result, the ML method is used to analyze the suggested topology.

Here, an optical surface plasmon-based structure is presented and analyzed for RI sensing applications. The presented topology consists of an MIM WG, a U-shaped resonator (USR), and an inverted U-shaped resonator (IUSR). To simulate the structure, the FDTD is utilized. The results show that the designed structure generates two FR modes with sensitivity values of 571.4 and 872.9 nm/RIU for the lower and upper FR modes, respectively. Also, the maximum FoM value is obtained for the lower FR mod that equals 14,987 RIU⁻¹. Furthermore, ML analysis is used to predict transmittance behavior. In other words, utilizing the Extreme Randomized Tree (ERT) regression model (RM) the transmittance values at intermediated wavelengths are forecasted. Using this method reduces the needed resources by 90%.

The next parts are ordered as follows: Part 2 shows the design procedure and FDTD simulation results of the suggested sensor. The ML RM is introduced and used for the presented structure in part 3. Part 4 compares the results with other similar works, and the last part is the conclusion.

Design procedure and simulation results

Figure 1 plots the designed surface plasmon-based RIS structure. The suggested structure comprises a USR coupled to an IUSR, both coupled to an MIM WG, and it is symmetrical about the centerline. The values of the defined geometrical dimensions equal l_1 =75, l_2 =40, l_3 =50, l_4 =100, l_5 =240, s=100, g=25, and w=100 (all in nm). The insulator and metal materials utilized for the presented sensor are air and silver, respectively. The air material has the relative permittivity of ε_d =1. Furthermore, the Drude model defines the relative permittivity of silver⁴⁴.

$$\varepsilon_{\rm m}(\omega) = \varepsilon_{\infty} - \frac{\omega_{\rm p}^2}{\omega(\omega + \mathrm{j}\gamma)}$$
(1)

In Eq. 1, ϵ_{∞} =3.7 denotes the medium dielectric constant for the infinite frequency. Also, $\omega_p=1.38\times 10^{16}$ Hz is the bulk plasma frequency, ω shows the angular frequency of incident light, and $\gamma=2.73\times 10^{13}$ Hz demonstrates the electron collision frequency.

Figure 2 illustrates the transmission curve of the proposed RIS (Fig. 1), which is obtained using the FDTD method. It is found that two FR modes with sharp edges appear in a wide wavelength range. In Fig. 2, the FR peaks and valleys are labeled with λ_{p1} =659 nm, λ_{p2} =871 nm, and λ_{v1} =598 nm, λ_{v2} =891 nm, respectively. The transmittance values of λ_{p1} and λ_{p2} are 59.9% and 70.8%, respectively. Furthermore, the transmittance values of λ_{v1} and λ_{v2} are almost near zero.

In the next step, the field profiles of $|H_z|$ for the RIS at peaks and valleys of the FR modes are represented in Fig. 3. As observed, two valley wavelengths of 598 and 891 nm do not achieve the right (output) port, while the peak resonance wavelengths of 659 and 871 nm transmit to this port. As observed in Fig. 3b, the energy at $\lambda_{\rm p1}$ = 659 nm is mainly concentrated within both USR and IUSR. Furthermore, Fig. 3c shows that for $\lambda_{\rm p2}$ = 871 nm, the most energy is only focused on the USR. It means that both resonators play a key role in the formation of the first peak, while the USR has a more significant influence on the formation of the second peak. In the following, this issue can be seen more clearly by calculating the transmission spectra of each resonator and waveguide separately.

To more accurately investigate the two generated FR modes, the two building block structures of the MIM WG coupled to IUSR (Structure 1) and USR (Structure 2) are also simulated separately, and their transmission

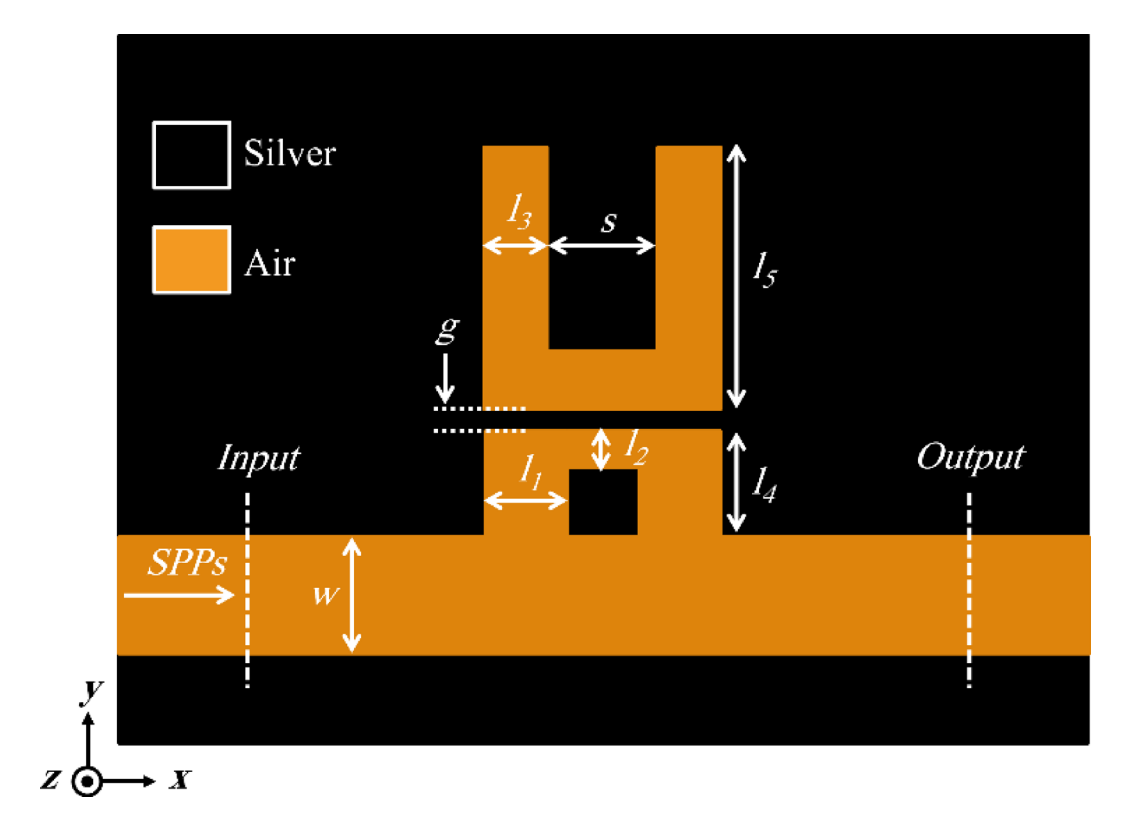


Fig. 1. The schematic of the RIS.

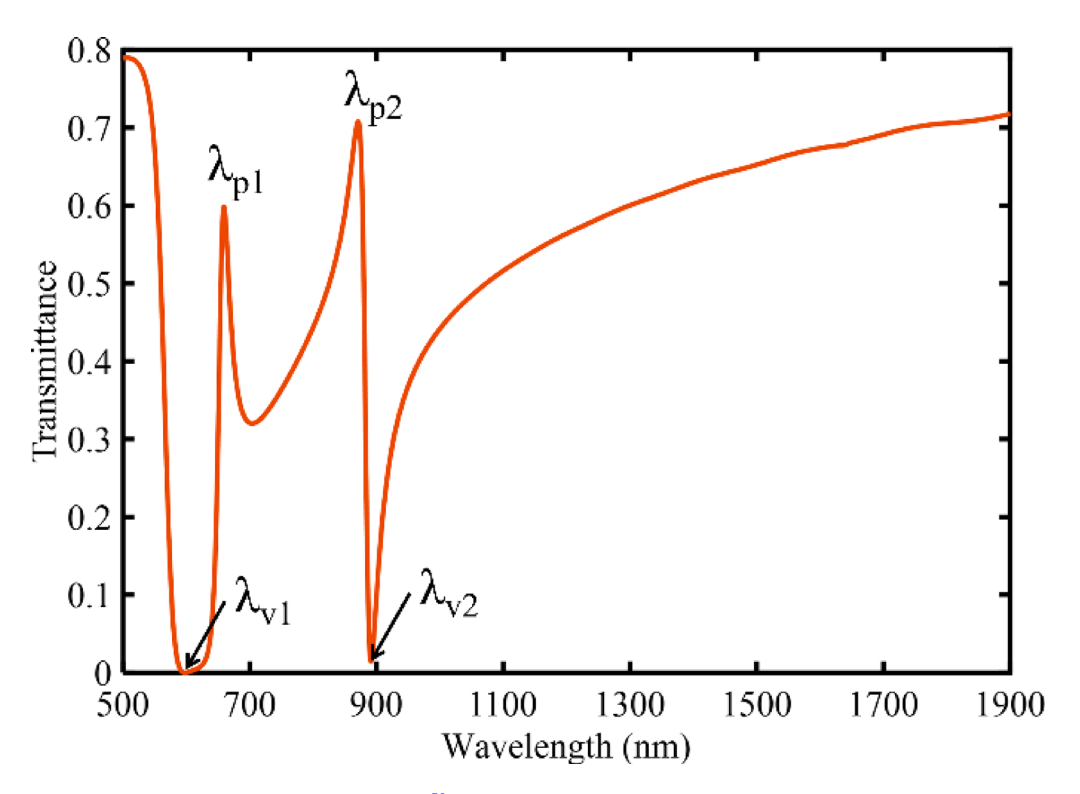


Fig. 2. Transmission spectrum of the RIS⁵⁸.

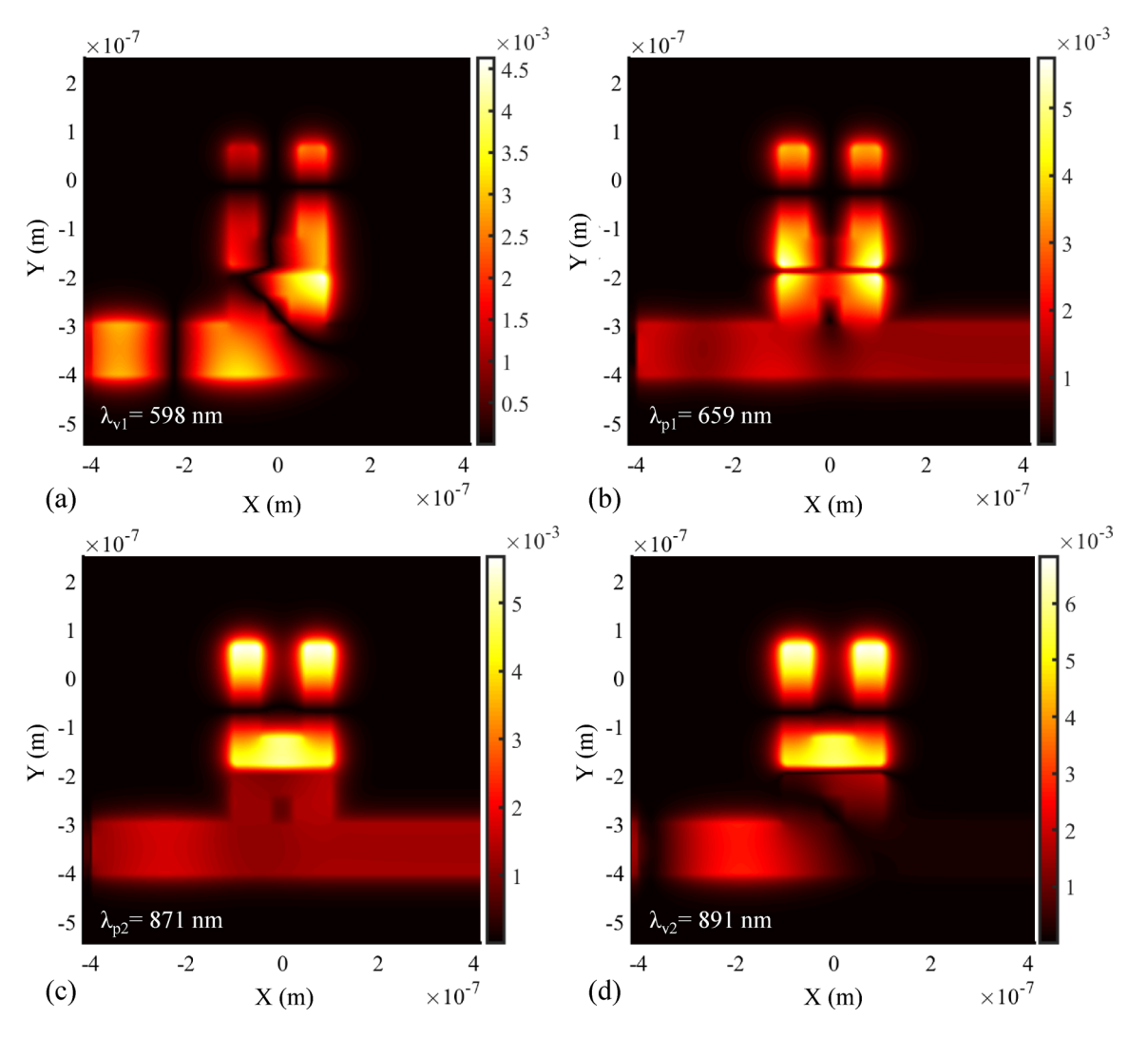


Fig. 3. Field profile of $|H_z|$ for the RIS at (a) λ_{v1} , (b) λ_{p1} , (c) λ_{p2} , and (d) λ_{v2} . (These figures are obtained by the "Lumerical 2020 R2.4. FDTD solutions" software)⁵⁸.

spectra are compared to the transmission curve of the proposed RIS in a single figure. Figure 4a,b show the schematic topologies of Structure 1 and Structure 2, respectively. Also, the transmission curves of the building blocks and the main RIS are presented in Fig. 4c.

The transmission curve of Structure 1 (IUSR coupled to the MIM WG) is presented by a green dotted line. It can be observed that Structure 1 creates a wide notch at a wavelength of 620 nm. Also, the transmission curve of Structure 2 (USR coupled to the MIM WG) is displayed by a black dot-dash line. As seen, two narrow notches at wavelengths of 634.2 and 879.4 nm are generated by Structure 2.

The suggested RIS is designed by combining both basic structures (Structure 1 and Structure 2), and its transmission spectrum is illustrated by an orange solid line. By the interaction between the broadband mode of Structure 1 and the narrowband modes of Structure 2, the two FR modes mentioned above are produced.

After designing the sensor structure, its RI sensing performance is examined. The transmission spectra of various filling media with the RI from 1 to 1.05 for Δn = 0.01 is presented in Fig. 5a. It indicates that when the RI of the analyte (insulator media) is increased, the transmittance curve shifts to higher wavelengths, regularly. In order to quantitatively evaluate optical sensors, various parameters have been defined. One of the most important parameters is sensitivity which can be given by⁴⁵:

$$S = \Delta \lambda / \Delta n \, \left(\frac{\text{nm}}{\text{RIU}} \right) \tag{2}$$

In Eq. 2, $\Delta\lambda$ and Δn demonstrate the shift of the resonance wavelength and the variation of the RI, respectively. Also, RIU is the RI unit. To calculate the sensitivity of the RIS, the data points of λ_{v1} and λ_{v2} are fitted by linear functions (Fig. 5b,c). The obtained linear functions for λ_{v1} and λ_{v2} are given in Eqs. 3 and 4, respectively.

$$\lambda_{v1} = 571.4n + 26.22 \tag{3}$$

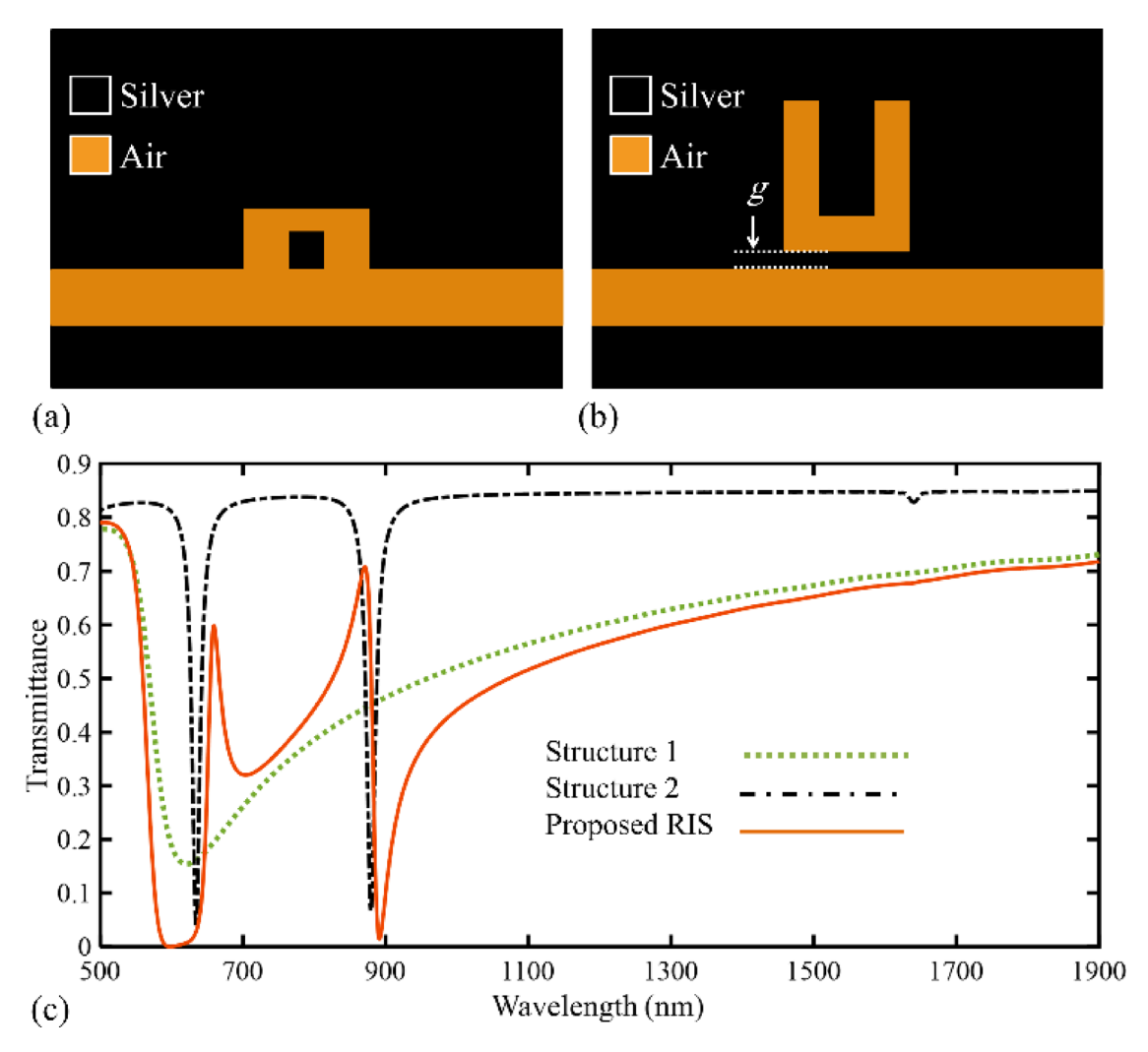


Fig. 4. The schematic of (a) Structure 1, (b) Structure 2. (c) The transmission spectra of Structure 1, Structure 2, and the RIS⁵⁸.

$$\lambda_{v2} = 872.9n + 18.1 \tag{4}$$

The slops of the linear functions ($\Delta V \Delta n$) are the RI sensitivity values at valley wavelengths. It can be concluded that the RI sensitivity for λ_{v1} and λ_{v2} are 571.4, and 872.9 nm/RIU, respectively. As observed, sensitivity is a parameter that specifies the value of wavelength shift for a determined RI variation, and it cannot show the resolution of a sensor³⁴. As a result, another more comprehensive parameter to evaluate the sensors' performance is the FoM parameter. This factor is defined as Eq. 5 for sensors with FR spectra⁴⁵.

$$FoM = \Delta T / \Delta n.T \text{ (RIU}^{-1})$$
(5)

In Eq. 5, Δ T, Δ n, and T are the change of the transmittance, the change of the RI, and the transmittance of the system, respectively. Based on Eq. 5, for the RIS designed in this paper, the FoM distribution of the wavelength is obtained (Fig. 6). Figure 6 shows that the maximum FoM value is obtained for λ_{v1} = 598 nm which equals 14,993 RIU⁻¹. It is worth mentioning that the FoM value obtained for λ_{v2} = 891 nm is 2178 RIU⁻¹. Therefore, the first valley wavelength with the highest FoM is considered for the sensing application of the designed RIS. Considering the remarkable sensitivity and FoM values obtained for the presented topology, it can be a suitable option for RI sensing.

Since the geometrical parameters of the suggested RIS can affect its transmission properties, the transmission performance for numerous values of some parameters $(l_1, l_2, l_3, \text{ and } g)$ is investigated here. The first column of Fig. 7a,d,g,j displays the transmission curves of the RIS for various values of l_1 , l_2 , l_3 , and g, respectively. Furthermore, the relationship between the FoM and various values of mentioned parameters for λ_{v1} and λ_{v2} are shown in the second column of Fig. 7b,e,h,k and the third column of Fig. 7c,f, i,l, respectively. Figure 7a displays that when the value of l_1 is increased, the locations of both FR modes are relatively constant, while Fig. 7b,c demonstrate that increasing l_1 increases the FoM of λ_{v1} initially and then decreases, and decreases the FoM of λ_{v2} . As discussed, the wavelength of λ_{v1} is chosen for sensing performance, and on the other hand, although the

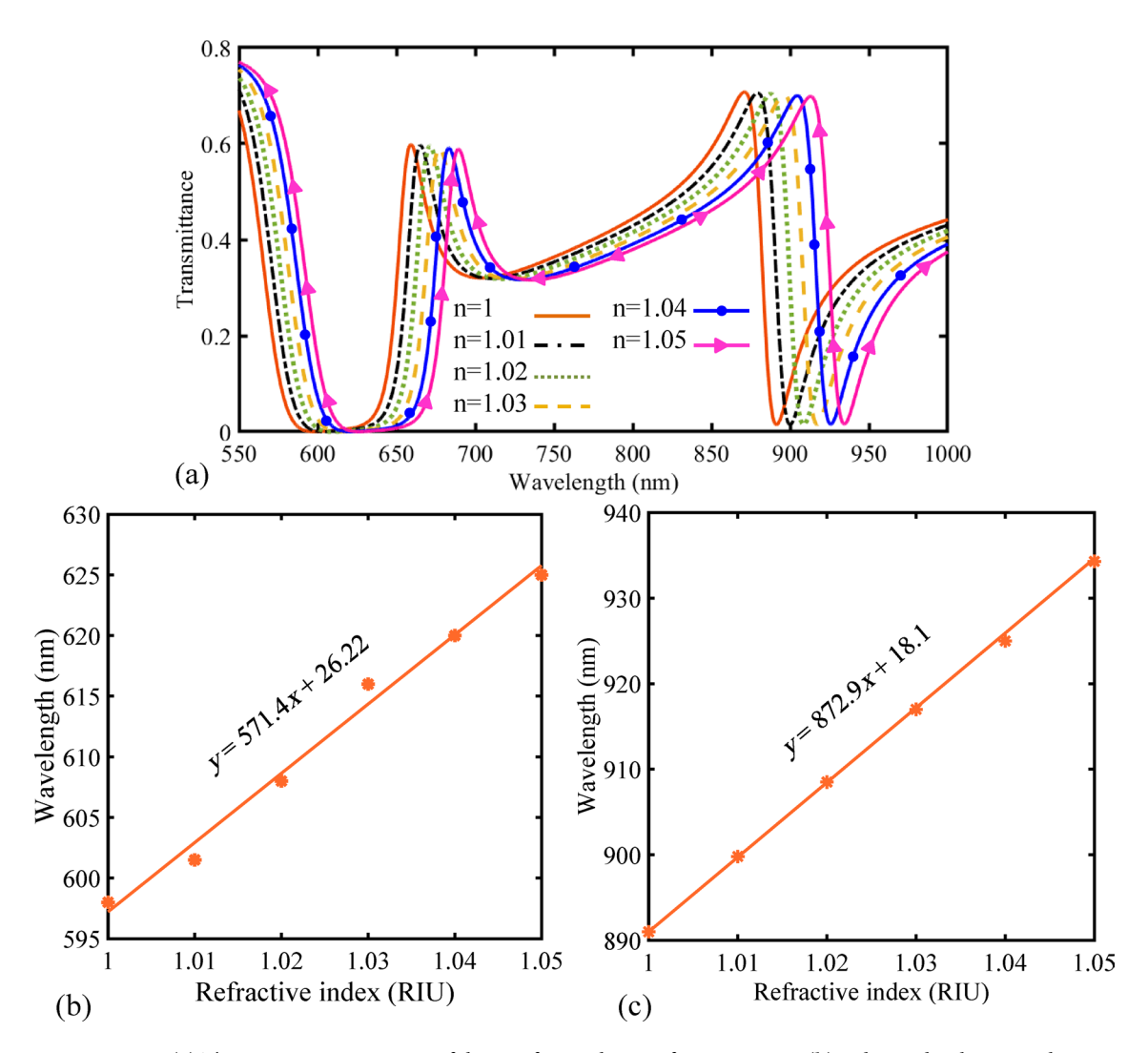


Fig. 5. (a) The transmission spectra of the RIS for RI changes from 1 to 1.05, (b) Relationship between the wavelengths of λ_{v2} and various values of the RI, (c) Relationship between the wavelengths of λ_{v2} and various values of the RI⁵⁸.

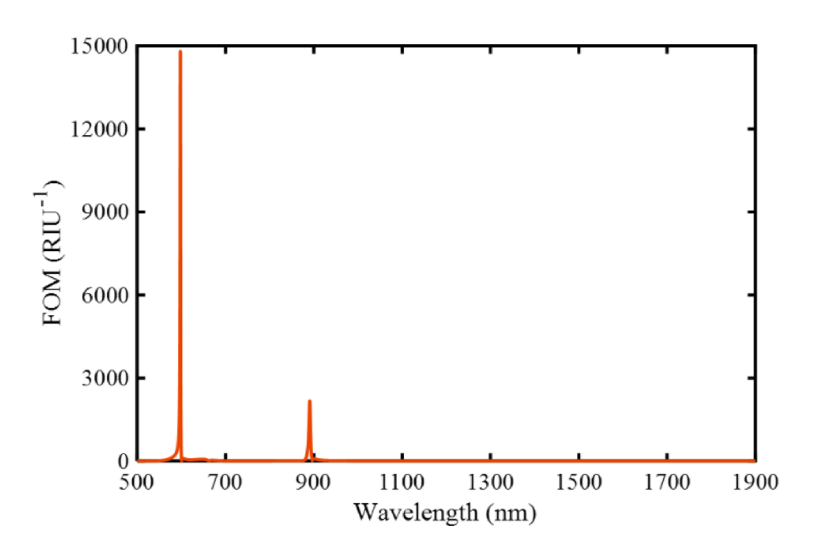


Fig. 6. The FoM values of the RIS⁵⁸.

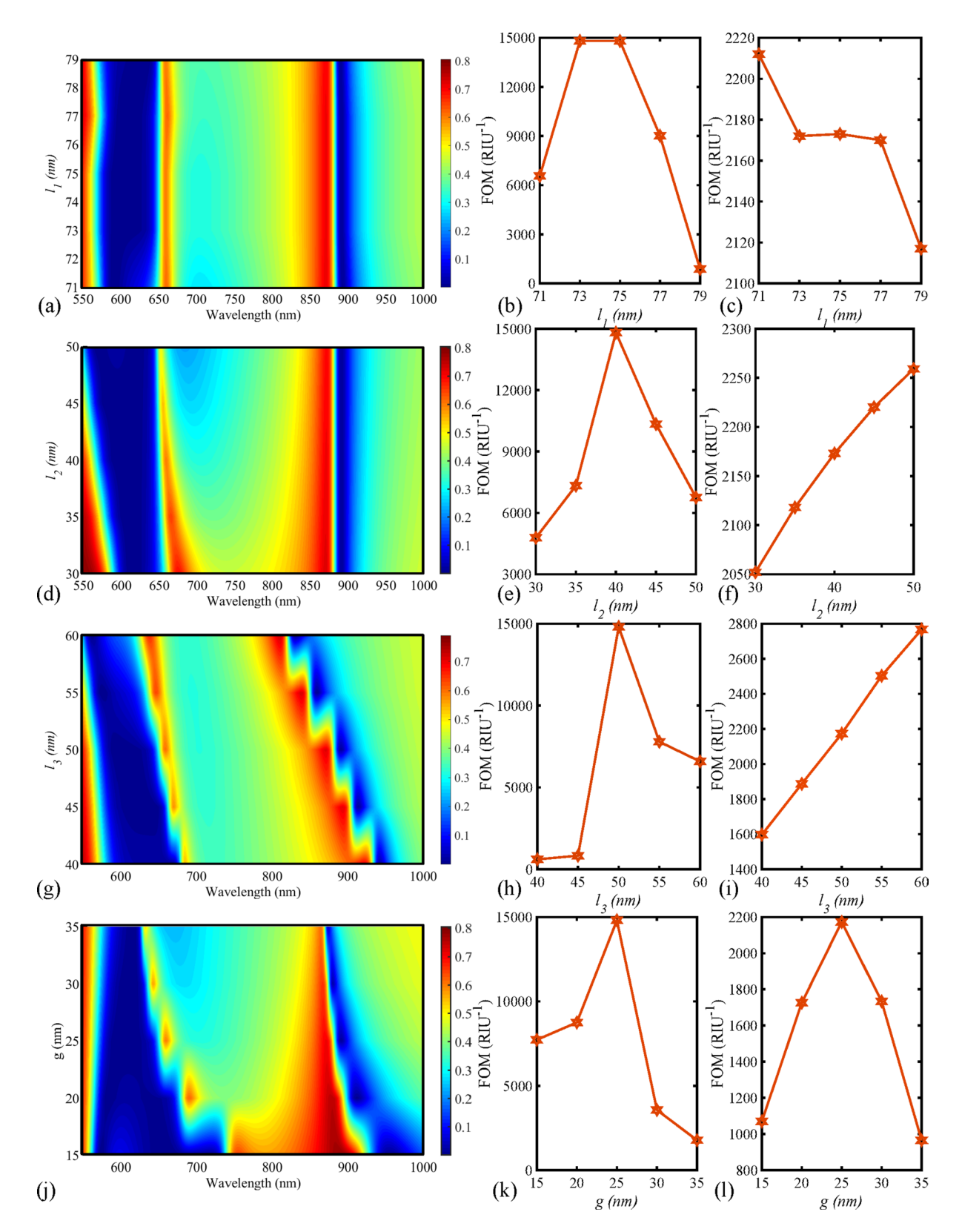


Fig. 7. Transmittances of the RIS for various values of (a) l_1 , (d) l_2 (g) l_3 , (j) g. Relationship between the FoM and various values of (b) l_1 , (e) l_2 (h) l_3 , (k) g for λ_{v1} . Relationship between the FoM and various values of (c) l_1 , (f) l_2 (i) l_3 , (l) g for λ_{v2}^{58} .

FoM of λ_{v_2} also changes, the range of these variations is much smaller than the FoM of λ_{v_1} . Consequently, the value of 75 nm for l_1 , which causes the highest FoM for λ_{v_1} is chosen.

Figure 7d shows that increasing l_2 shifts the first valley wavelength to the lower wavelengths, while the location of the second valley wavelength is constant. Also, by increasing l_2 , the highest FoM of λ_{v1} is obtained at l_2 = 40 nm and the FoM of λ_{v2} increases (Fig. 7e,f). Therefore, for the same reasons as in the previous case (variations of l_1), l_2 = 40 nm is chosen. Variations of l_3 are demonstrated in Fig. 7g–i. Figure 7g demonstrates that changing the l_3 value varies the locations of both FR modes. In other words, variations of l_3 result in a plasmonic structure with tunable resonance mods. The variations of the FoM of λ_{v1} and λ_{v2} are similar to the previous case (l_2). Figure 7h,i show these cases. As a result, l_3 = 50 nm is chosen. The gap of g is the last parameter in which its variation is studied (Fig. 7j–l). Figure 7j indicates that increasing the g value shifts the FR modes to the higher wavelengths. Furthermore, the FoM values of both FR modes increase initially and then decrease when the g value is increased (Fig. 7k,l). The highest FoM values for both modes occur at g = 25 nm which is selected.

Machine learning analysis

As known, using FDTD and FEM simulation methods for optical systems is time-consuming and needs extra memory, computational power, and processing time. Therefore, utilizing a method that can reduce the resources and time required to simulate is necessary. ML techniques such as the ERT RM can solve these challenges by predicting essential parameters and specifying missing values. Therefore, this section discusses the RMs briefly and shows how these techniques can reduce the needed resources for the proposed sensor structure by 90%. Regression analysis specifies dependent parameter values (transmittance) according to independent parameter values (wavelength), and uses three steps as follows:

Step 1: Simulating the RIS utilizing a larger wavelength's step size.

Step 2: Training the RM with the simulation data.

Step 3: Predicting the transmittance of middle wavelengths utilizing the trained model.

Two vital parameters for the regression analysis used in this paper (ERT model) are the minimum needed sample size for node splitting (n_{min}) and the number of randomly selected properties at each node (K). The parameter of K=1.....p is used to determine the property strength applied to compute the goal. Here p shows the independent variables utilized to anticipate the goal parameter. To have more precision, the K value should be larger⁴⁶.

In this paper, to forecast the transmittance, six parameters are used. They are l_1 , l_2 , l_3 , g, n, and wavelength (λ). It is worth mentioning that the value of n_{\min} is considered 3. This can be explained below. First, all values between 2 and 10 are considered for n_{\min} , and no significant difference is observed in the outputs. Since different figures for various values of five selected parameters (l_1 , l_2 , l_3 , g, and n) are given in the following, to reduce the number of similar figures and reduce the number of pages, only one case ($n_{\min} = 3$) is reported. It is worth mentioning that the scope of K is ($1 \le K \le$ total number of attributes). Since the number of input features of the problem equals one (we only have one input that is wavelength (λ)), k = 1 is considered here. In the ERT RM, a set of "m" unpruned regression trees is produced. They are RT_1 , RT_2 , RT_3 , ..., RT_m . By calculating the total of each tree's forecasts and taking the arithmetic mean of the outcomes, the final prediction is attained. Equation 6 demonstrates it⁴⁷.

$$Predicted output = \sum_{j=1}^{m} RT_{j}(x)$$
 (6)

In Eq. 6, m is the number of trees, and x demonstrates the value of the independent parameter. Some performance indices may be utilized to calculate the accuracy of the trained ERT RM. These indices are R-Square Score (R^2 S), Adjusted R Square Score (Adj- R^2 S), Root Mean Squared Error (RMSE), and Mean Absolute Percentage Error (MAPE) which are expressed by Eqs. 7–10 47

$$R^{2}s = 1 - \frac{\sum_{i=1}^{N} (Predicted Value_{i} - Actual Value_{i})^{2}}{\sum_{i=1}^{N} (Actual Value_{i} - Average Target Value_{i})^{2}}$$
(7)

$$Adj - R^{2}s = 1 - \frac{(1 - R^{2}s)(N - 1)}{N - p - 1}$$
(8)

$$RMSE = \sqrt{\frac{1}{N} \sum_{i=1}^{N} (Actual \, Value_i - Predicted \, Value_i)^2} \tag{9}$$

$$MAPE = \frac{1}{N} \sum_{i=1}^{N} \left[\frac{Actual \, Value_i - Predicted \, Value_i}{Actual \, Value_i} \right] * 100 \tag{10}$$

In these Equations, N illustrates the total number of samples that were used in the validation of the RM. As mentioned, the ERT RM is used to predict the transmission value in this work. This model is applied for the test case of 10% (TC-10). Two distinct subsets of the FDTD-generated data are utilized in TC-10. In the first subset, 10% of the simulation data are selected for training the ERT RM. It is worth mentioning that these data are chosen with equal row spacing. The other 90% of the simulation data are considered for the accuracy of the model's predictive (the second subset).

Figure 8 displays the heat map of the Adj-R²S of the ERT RM for $n_{\min} = 3$. It is worth noting that in this figure, all values are rounded to four decimal places, and the exact values are shown in parentheses. Adj-R²S for different values of l_1 , l_2 , l_3 , g, and n are depicted in Fig. 8a–e, respectively. As observed, Adj-R²S values are close to 1. As a result, it can be said that high prediction accuracy is obtained. In other words, a tight link exists between simulated (actual) and predicted values.

Figure 9 illustrates the predicted values by the ERT RM versus the actual values of the transmission curves for various values of l_1 (Fig. 9a), l_2 (Fig. 9b), l_3 (Fig. 9c), g (Fig. 9d), and the RI of n (Fig. 9e). The obtained results for all parameters indicate that predicted and actual values are matched. Therefore, the high accuracy of the prediction is also concluded from this figure.

The RMSE generated for various values of all aforementioned parameters $(l_1, l_2, l_3, g, \text{ and n})$ using comparative bar charts are demonstrated in Fig. 10. Figure 10a,d,e displays that the RMSE value less than 0.0018 is obtained for all various values of l_1 , g, and n. Furthermore, for all different values of l_2 and l_3 , the RMSE value less than 0.002 is attained. In fact, these figures show the low error prediction error.

Finally, the predicted versus the simulated transmittances of the suggested RIS are shown in Fig. 11. This figure shows that both curves are in good agreement. Consequently, using the ML-based ERT RM can reduce the simulation time for designing the plasmonic RIS by 90%.

Comparisons and discussions

To design the RIS presented here, the 2D FDTD simulation technique is used. This means that the thickness of the silver slab is considered to be infinite. As known, 3D simulations are more time-consuming and more complex than 2D simulations. Accordingly, it is more prevalent to use 2D topologies for plasmonic structures^{48–50}. It is

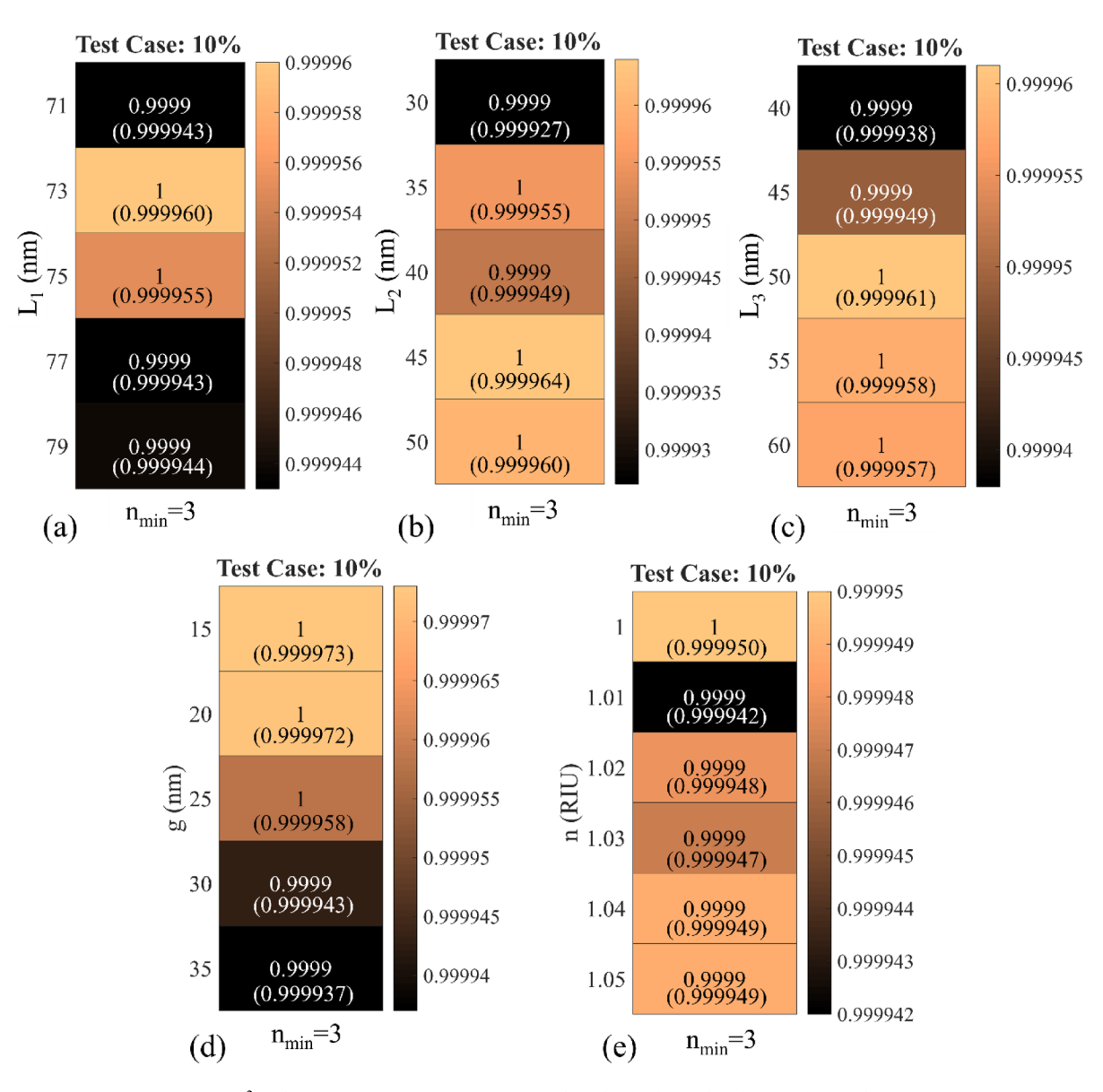


Fig. 8. Adj-R²S of ERT RM using various values of (a) l_1 , (b) l_2 , (c) l_3 , (d) g, and (e) n for TC-10.

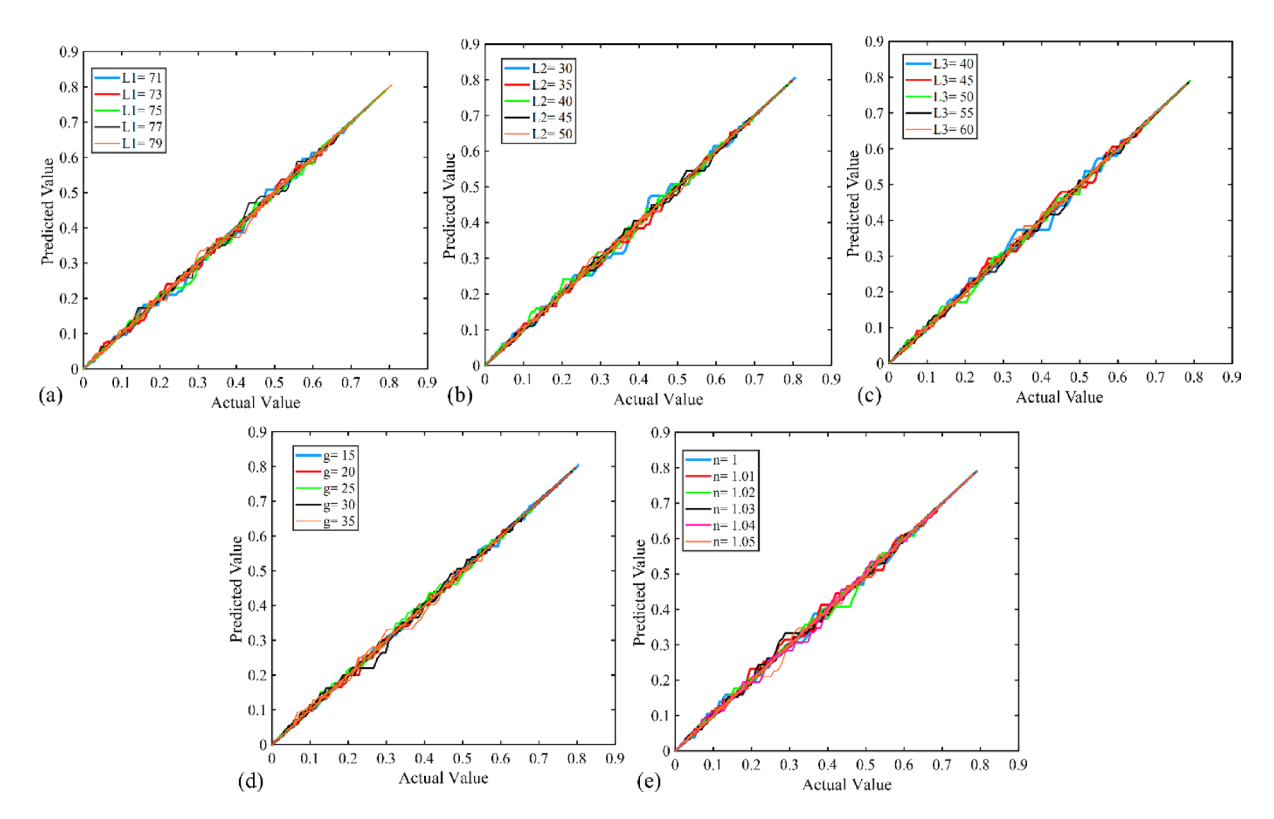


Fig. 9. Predicted vs actual values using various values of (a) l_1 , (b) l_2 , (c) l_3 , (d) g, and (e) n for TC-10.

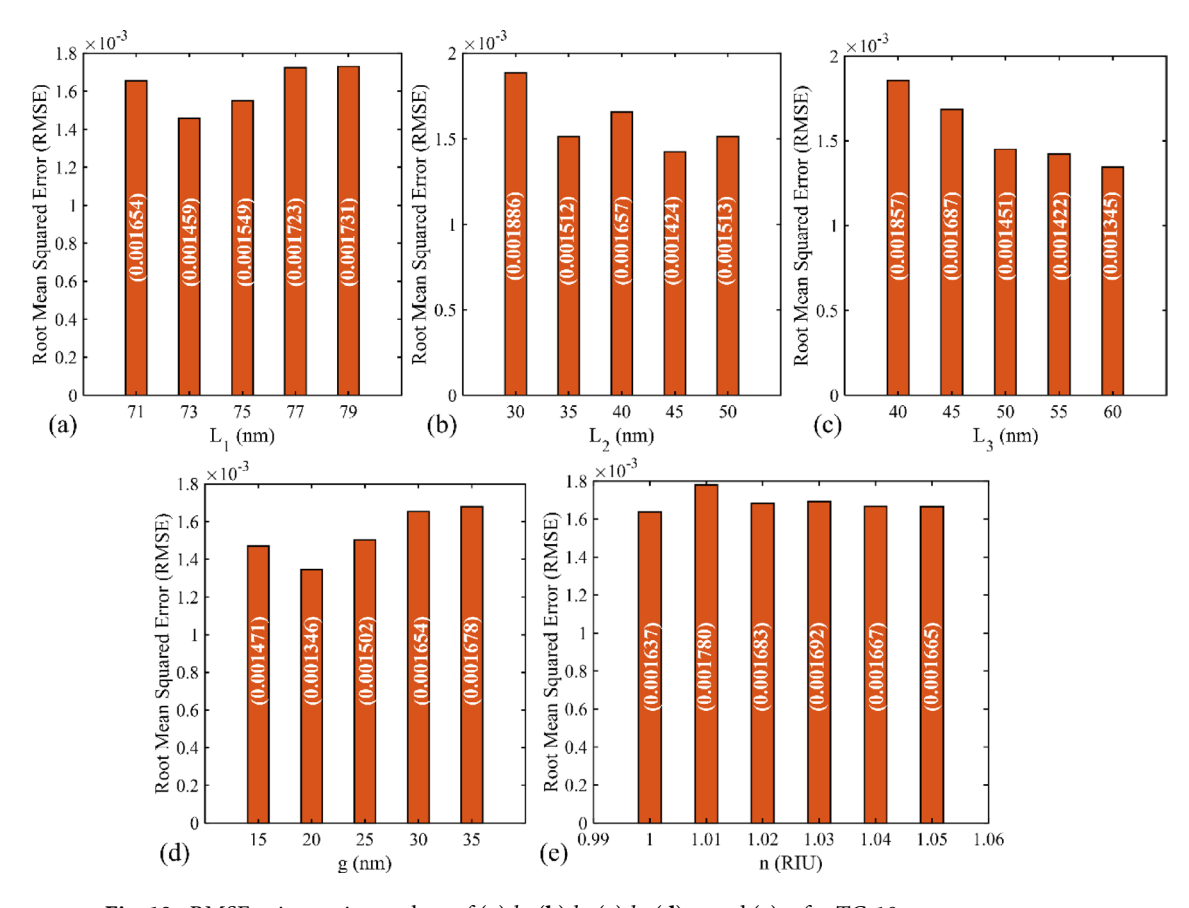


Fig. 10. RMSE using various values of (a) l_1 , (b) l_2 , (c) l_3 , (d) g, and (e) n for TC-10.

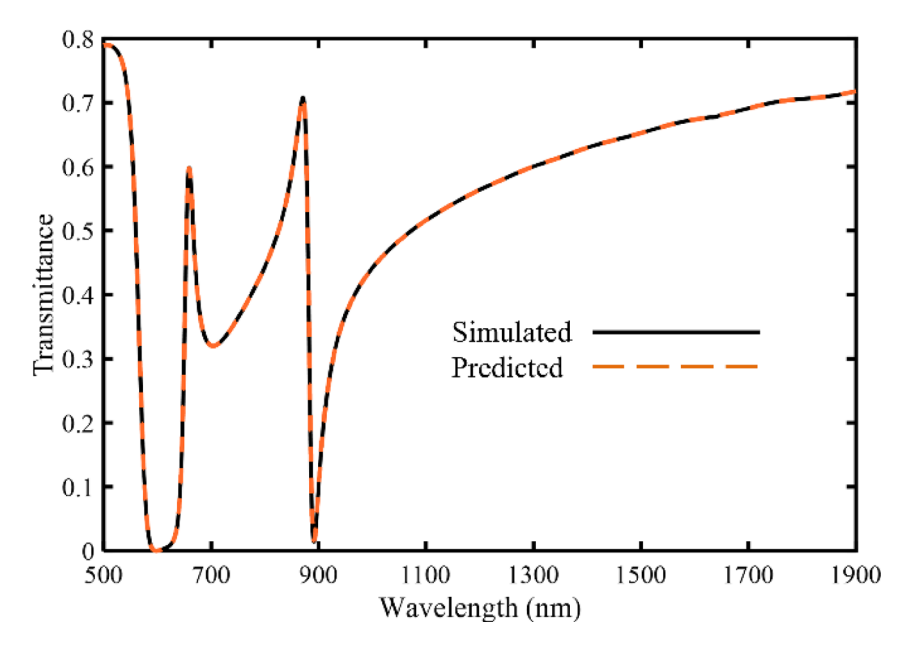


Fig. 11. Predicted vs simulated transmission spectra of the RIS⁵⁸.

Ref	S (nm/RIU)	FOM _{max} (RIU ⁻¹)	Year
Ref ⁵¹	4459.05	297.67	2024
Ref ⁵²	1222	175.9	2023
Ref ⁵³	1435	87.3	2023
Ref ⁵⁴	1636	33,562	2022
Ref ⁵⁵	1048.6	-	2022
Ref ⁵⁶	1200	191.6	2021
Ref ⁵⁷	880	964	2018
This work	571.4	14,987	-

Table 1. Comparisons of the suggested RIS with other papers.

worth mentioning that most such topologies can be generalized to 3D structures with finite thicknesses. As a result, the suggested surface plasmon-based sensor is also realized based on 2D simulations. Furthermore, air with the dielectric permittivity of 1 and silver are used as insulator and metal materials in the proposed sensor. The dielectric permittivity of silver is characterized by the Drude model. As known, the Drud model is one of the well-known models used to describe the dielectric coefficient of silver in most works, and it can be said that this model can provide an acceptable approximation of the behavior of silver metal in practical situations. The perfectly matched layer (PML) boundary condition is utilized to surround the simulation domain. The thickness of the PML is 200 layers. Furthermore, the mesh size for the total structure equals 2 nm.

It is worth saying that it is currently not possible for us to confirm the obtained results by fabrication data. Since it is not possible to fabricate such devices in our country, the idea of realizing a plasmonic sensor is only proposed in this paper, and it tries to carefully examine the performance of the suggested topology using the well-known FDTD method. Furthermore, ML analysis is utilized to predict transmittance behavior. In other words, using the ERT RM the transmittance values at intermediated wavelengths are forecasted. Applying this method reduces the needed resources by 90%.

In this section, the rest is to compare the proposed design with other similar sensors. For this purpose, Table 1 is suggested to compare the important parameters that include the sensitivity (S) and the maximum value of the FoM (FoM $_{\rm max}$). The sensitivity and FoM values of all references in this table are calculated by Eqs. 2 and 5, respectively.

As discussed, although sensitivity can be a main parameter for the sensor's performance, it cannot show the sensor's resolution, and the FoM parameter is more comprehensive. Therefore, having a high FoM value is more important. For example, Table 1 demonstrates that the sensor proposed in Ref. ⁵¹ has the highest sensitivity value among the works, while it does not have a high FoM value compared to other works. It is clear that the RIS proposed in this paper simultaneously has optimal features such as high sensitivity and FoM values compared to other similar works. Accordingly, the results indicate that the sensor topology presented here may be applied to numerous RI sensing demands in biomedical, chemical, and environmental fields.

Conclusion

In summary, this article presents a surface plasmon-based RIS composed of a USR, an IUSR, and an MIM WG. According to the FDTD simulations, the design produces two FR modes. The most suitable values of sensitivity and FoM are 571.4 nm/RIU and 14,987 RIU $^{-1}$ at the wavelength of $\lambda_{\rm v1}$ = 598 nm. Also, the ML-based ERT RM is applied to learn transmission performance and forecast transmittance values for middle wavelengths. The Adj-R²S nears1, illustrating the prediction efficiency of the ERT RM in calculating the transmittance values in TC-10. Applying this ML-based method reduces needed resources and simulation time by 90%. The proposed RIS designed with the ERT model can be used for RI measurement in biomedical, chemical, and environmental applications.

Data availability

The calculated results during the current study are available from the corresponding author on reasonable request.

Received: 26 February 2025; Accepted: 23 June 2025

Published online: 04 July 2025

References

- 1. Su, M., Qi, Y., Li, H., Zhang, S. & Wang, X. A dual-purpose sensor with a sawtooth U-shaped cavity and a rectangle-shaped cavity in a MIM waveguide structure. *Phys. Scr.* **98**, 085520 (2023).
- 2. Hutter, E. & Fendler, J. H. Exploitation of localized surface plasmon resonance. Adv. Mater. 16, 1685-1706 (2004).
- Maier, S. A. & Atwater, H. A. Plasmonics: Localization and guiding of electromagnetic energy in metal/dielectric structures. J. Appl. Phys. 98 (2005).
- 4. Maier, S. (Springer, 2007).
- 5. Gramotney, D. K. & Bozhevolnyi, S. I. Plasmonics beyond the diffraction limit. Nat. Photon. 4, 83-91 (2010).
- 6. Rinaldi, G. Nanoscience and technology: a collection of reviews from nature journals. Assembly Autom. 30 (2010).
- 7. Khani, S. & Rezaei, P. Optical sensors based on plasmonic nano-structures: A review. Heliyon 10, 24 (2024).
- 8. Ebadi, S. M., Khani, S. & Örtegren, J. Design of miniaturized wide band-pass plasmonic filters in MIM waveguides with tailored spectral filtering. *Opt. Quant. Electron.* **56**, 1–24 (2024).
- 9. Elbialy, S., El-den, B. & Ashraf, E. Realizing high-performance four active plasmonic filters using a single structure. Sci. Rep. 14, 29465 (2024).
- 10. Khani, S., Danaie, M. & Rezaei, P. Double and triple-wavelength plasmonic demultiplexers based on improved circular nanodisk resonators. *Opt. Eng.* 57, 107102–107102 (2018).
- Wang, Z. et al. Plasmonic demultiplexer with tunable output power ratio based on metal-dielectric-metal structure and E7 liquid crystal arrays. *IEEE Photon. J.* 12, 1–10 (2020).
- Khani, S., Farmani, A. & Mir, A. Reconfigurable and scalable 2, 4-and 6-channel plasmonics demultiplexer utilizing symmetrical rectangular resonators containing silver nano-rod defects with FDTD method. Sci. Rep. 11, 13628 (2021).
- 13. Chang, K.-W. & Huang, C.-C. Ultrashort broadband polarization beam splitter based on a combined hybrid plasmonic waveguide. Sci. Rep. 6, 19609 (2016).
- Wang, X.-Y., Liu, J.-M., Yang, Y.-J. & Zhang, D.-L. Compact polarization beam splitter based on metal-capped thin-film LiNbO3on-insulator plasmonic waveguide. Opt. Laser Technol. 172, 110491 (2024).
- 15. Alipour, A. H., Khani, S., Ashoorirad, M. & Baghbani, R. Trapped multimodal resonance in magnetic field enhancement and sensitive THz plasmon sensor for toxic materials accusation. *IEEE Sens. J.* 23, 14057–14066 (2023).
- 16. Asl, A. B., Ahmadi, H. & Rostami, A. A novel plasmonic metal–semiconductor–insulator–metal (MSIM) color sensor compatible with CMOS technology. *Sci. Rep.* 13, 14029 (2023).
- 17. Rahad, R., Joy, J. D., Rahman, M. S., Emon, M. J. H. & Haque, M. A. Miniaturized plasmonic sensor with dual-function capability for pressure and flow rate detection at subwavelength levels. *IEEE Sens. J.* (2025).
- 18. Butt, M. A. & Piramidowicz, R. Orthogonal mode couplers for plasmonic chip based on metal-insulator-metal waveguide for temperature sensing application. Sci. Rep. 14, 3474 (2024).
- Alves Oliveira, I., Gomes de Souza, I. L. & Rodriguez-Esquerre, V. F. Design of hybrid narrow-band plasmonic absorber based on chalcogenide phase change material in the infrared spectrum. Sci. Rep. 11, 21919 (2021).
- Ebadi, S. M. & Khani, S. Design of a tetra-band MIM plasmonic absorber based on triangular arrays in an ultra-compact MIM waveguide. Opt. Quant. Electron. 55, 482 (2023).
- 21. Swillam, M. A., Zaki, A. O., Kirah, K. & Shahada, L. A. On chip optical modulator using epsilon-near-zero hybrid plasmonic platform. Sci. Rep. 9, 6669 (2019).
- Singh, L. et al. MIM waveguide based multi-functional plasmonic logic device by phase modulation. IEEE Trans. Nanotechnol. (2024).
- 23. Chang, K.-H., Lin, Z.-H., Lee, P.-T. & Huang, J.-S. Enhancing on/off ratio of a dielectric-loaded plasmonic logic gate with an amplitude modulator. Sci. Rep. 13, 5020 (2023).
- 24. Zhang, Z.-K. *et al.* All-optical single-channel plasmonic logic gates. *Nano Lett.* (2025).
- Khani, S., Danaie, M. & Rezaei, P. Plasmonic all-optical metal-insulator-metal switches based on silver nano-rods, comprehensive theoretical analysis and design guidelines. *J. Comput. Electron.* 20, 442–457 (2021).
- 26. Khani, S., Farmani, A. & Rezaei, P. Optical resistance switch for optical sensing. Opt. Imaging Sens. Mater. Devices Appl. 83-122 (2023)
- Zafar, R., Nawaz, S., Singh, G., d'Alessandro, A. & Salim, M. Plasmonics-based refractive index sensor for detection of hemoglobin concentration. IEEE Sens. J. 18, 4372–4377 (2018).
- 28. Khani, S. & Hayati, M. Optical biosensors using plasmonic and photonic crystal band-gap structures for the detection of basal cell cancer. Sci. Rep. 12, 5246 (2022).
- Butt, M., Khonina, S. & Kazanskiy, N. Metal-insulator-metal nano square ring resonator for gas sensing applications. Waves Random Complex Media 31, 146–156 (2021).
- 30. Rahad, R., Rakib, A., Haque, M. A., Sharar, S. S. & Sagor, R. H. Plasmonic refractive index sensing in the early diagnosis of diabetes, anemia, and cancer: An exploration of biological biomarkers. *Results Phys.* 49, 106478 (2023).
- 31. Yang, X., Hua, E., Su, H., Guo, J. & Yan, S. A nanostructure with defect based on Fano resonance for application on refractive-index and temperature sensing. Sensors 20, 4125 (2020).
- 32. Butt, M. A. Plasmonic sensor system embedded with orthogonal mode couplers for simultaneous monitoring of temperature and refractive index. *Plasmonics* 1–11 (2024).
- 33. Cao, Y. et al. Nanoscale refractive index sensor based on an MIM waveguide coupled to U-shaped ring resonator with three stubs for alcohol solution concentration detection. *Plasmonics* 19, 2421–2432 (2024).

- 34. Khani, S. & Hayati, M. An ultra-high sensitive plasmonic refractive index sensor using an elliptical resonator and MIM waveguide. Superlattices Microstruct. 156, 106970 (2021).
- 35. Sharma, Y., Zafar, R., Metya, S. K. & Kanungo, V. Split ring resonators-based plasmonics sensor with dual Fano resonances. *IEEE Sens. J.* 21, 6050–6055 (2020).
- 36. Al Mahmud, R., Faruque, M. O. & Sagor, R. H. A highly sensitive plasmonic refractive index sensor based on triangular resonator. Opt. Commun. 483, 126634 (2021).
- 37. Rashid, K. S., Tathfif, I., Yaseer, A. A., Hassan, M. F. & Sagor, R. H. Cog-shaped refractive index sensor embedded with gold nanorods for temperature sensing of multiple analytes. *Opt. Express* 29, 37541–37554 (2021).
- Chou Chao, C.-T. et al. Highly sensitive and tunable plasmonic sensor based on a nanoring resonator with silver nanorods. Nanomaterials 10, 1399 (2020).
- 39. Chen, Z. et al. Tunable high quality factor in two multimode plasmonic stubs waveguide. Sci. Rep. 6, 24446 (2016).
- 40. Shi, H. et al. Nanosensor based on Fano resonance in a metal-insulator-metal waveguide structure coupled with a half-ring. *Results Phys.* 21, 103842 (2021).
- 41. Karami, H., Karimi, S., Rahmanimanesh, M. & Farzin, S. Predicting discharge coefficient of triangular labyrinth weir using support vector regression, support vector regression-firefly, response surface methodology and principal component analysis. *Flow Meas. Instrum.* 55, 75–81 (2017).
- 42. Yan, R. et al. Design of high-performance plasmonic nanosensors by particle swarm optimization algorithm combined with machine learning. *Nanotechnology* 31, 375202 (2020).
- 43. Jain, P. et al. Machine learning assisted hepta band THz metamaterial absorber for biomedical applications. Sci. Rep. 13, 1792 (2023).
- Ebadi, S. M., Khani, S. & Örtegren, J. Ultra-compact multifunctional Surface plasmon device with tailored optical responses. Results Phys. 61, 107783 (2024).
- Wen, K., Chen, L., Zhou, J., Lei, L. & Fang, Y. A plasmonic chip-scale refractive index sensor design based on multiple Fano resonances. Sensors 18, 3181 (2018).
- Criminisi, A., Shotton, J. & Konukoglu, E. Decision forests: A unified framework for classification, regression, density estimation, manifold learning and semi-supervised learning. Found. Trends* Comput. Graph. Vis. 7, 81–227 (2012).
- 47. Jain, P. et al. Multiband metamaterial absorber with absorption prediction by assisted machine learning. *Mater. Chem. Phys.* **307**, 128180 (2023).
- 48. Chen, F., Zhang, H., Sun, L., Li, J. & Yu, C. Temperature tunable Fano resonance based on ring resonator side coupled with a MIM waveguide. Opt. Laser Technol. 116, 293–299 (2019).
- 49. Guchhait, S., Chatterjee, S., Chakravarty, T. & Ghosh, N. A metal-insulator-metal waveguide-based plasmonic refractive index sensor for the detection of nanoplastics in water. *Sci. Rep.* 14, 21495 (2024).
- 50. Khani, S. & Hayati, M. High resolution refractive index and temperature sensor with Fano resonance in disk and parenthesis-shaped plasmonic cavities. *Results Opt.* 19, 100816 (2025).
- Sun, Y., Qu, D., Ren, Y. & Li, C. Nanorods-enhanced MIM plasmonic sensor based on S-shaped waveguide coupled with ohmshaped and D-shaped resonators. *Physica E* 161, 115971 (2024).
- 52. Zhang, S. et al. Narrow-band notch filter and refractive index sensor based on rectangular-semi-annular cavity coupled with MIM waveguide structure. *Phys. Scr.* **98**, 085522 (2023).
- Wang, L. et al. Surface plasmon polaritons filter with transmission optimized based on the multimode interference coupled mode theory. *Plasmonics* 18, 493–502 (2023).
- 54. Rohimah, S. et al. Tunable multiple Fano resonances based on a plasmonic metal-insulator-metal structure for nano-sensing and plasma blood sensing applications. *Appl. Opt.* **61**, 1275–1283 (2022).
- 55. Liu, Y., Tian, H., Zhang, X., Wang, M. & Hao, Y. Quadruple Fano resonances in MIM waveguide structure with ring cavities for multisolution concentration sensing. *Appl. Opt.* **61**, 10548–10555 (2022).
- Ding, J. et al. Multiple Fano resonances based on clockwork spring-shaped resonator for refractive index sensing. Phys. Scr. 96, 125538 (2021).
- 57. Guo, Z. et al. Plasmonic multichannel refractive index sensor based on subwavelength tangent-ring metal-insulator-metal waveguide. Sensors 18, 1348 (2018).
- 58. Lumerical 2020 R2.4. FDTD solutions.

Acknowledgements

The authors would like to thank the journal editor and reviewers for their valuable comments. This research is founded by Semnan University, research [grant number T14031054].

Author contributions

Design, analysis, investigation, validation, writing—original draft preparation, and writing—review and editing: Shiva Khani, validation, writing—review and editing: Pejman Rezaei, machine learning analysis, validation, writing—review and editing: Mohammad Rahmanimanesh. All authors discussed the results and contributed to the final manuscript.

Declarations

Competing interests

The authors declare no competing interests.

Additional information

Correspondence and requests for materials should be addressed to S.K.

Reprints and permissions information is available at www.nature.com/reprints.

Publisher's note Springer Nature remains neutral with regard to jurisdictional claims in published maps and institutional affiliations.

Open Access This article is licensed under a Creative Commons Attribution-NonCommercial-NoDerivatives 4.0 International License, which permits any non-commercial use, sharing, distribution and reproduction in any medium or format, as long as you give appropriate credit to the original author(s) and the source, provide a link to the Creative Commons licence, and indicate if you modified the licensed material. You do not have permission under this licence to share adapted material derived from this article or parts of it. The images or other third party material in this article are included in the article's Creative Commons licence, unless indicated otherwise in a credit line to the material. If material is not included in the article's Creative Commons licence and your intended use is not permitted by statutory regulation or exceeds the permitted use, you will need to obtain permission directly from the copyright holder. To view a copy of this licence, visit http://creativecommons.org/licenses/by-nc-nd/4.0/.

© The Author(s) 2025